nanomaterials

MDPI

Article

Self-Consistent Model for the Compositional Profiles in Vapor–Liquid–Solid III–V Nanowire Heterostructures Based on Group V Interchange

Vladimir G. Dubrovskii

Faculty of Physics, St. Petersburg State University, Universitetskaya Emb. 13B, 199034 St. Petersburg, Russia; dubrovskii@mail.ioffe.ru

Abstract: Due to the very efficient relaxation of elastic stress on strain-free sidewalls, III–V nanowires offer almost unlimited possibilities for bandgap engineering in nanowire heterostructures by using material combinations that are attainable in epilayers. However, axial nanowire heterostructures grown using the vapor–liquid–solid method often suffer from the reservoir effect in a catalyst droplet. Control over the interfacial abruptness in nanowire heterostructures based on the group V interchange is more difficult than for group-III-based materials, because the low concentrations of highly volatile group V atoms cannot be measured after or during growth. Here, we develop a self-consistent model for calculations of the coordinate-dependent compositional profiles in the solid and liquid phases during the vapor–liquid–solid growth of the axial nanowire heterostructure $A_{x_0}B_{1-x_0}C/A_{x_1}B_{1-x_1}C$ with any stationary compositions x_0 and x_1. The only assumption of the model is that the growth rates of both binaries AC and BC are proportional to the concentrations of group V atoms A and B in a catalyst droplet, requiring high enough supersaturations in liquid phase. The model contains a minimum number of parameters and fits quite well the data on the interfacial abruptness across double heterostructures in $GaP/GaAs_xP_{1-x}/GaP$ nanowires. It can be used for any axial III–V nanowire heterostructures obtained through the vapor–liquid–solid method. It forms a basis for further developments in modeling the complex growth process and suppression of the interfacial broadening caused by the reservoir effect.

Keywords: nanowire heterostructures; VLS growth; group V interchange; compositional profiles; modeling

Citation: Dubrovskii, V.G. Self-Consistent Model for the Compositional Profiles in Vapor–Liquid–Solid III–V Nanowire Heterostructures Based on Group V Interchange. *Nanomaterials* **2024**, *14*, 821. https://doi.org/10.3390/nano14100821

Academic Editor: Patrick Fiorenza

Received: 22 March 2024
Revised: 29 April 2024
Accepted: 4 May 2024
Published: 7 May 2024

1. Introduction

III–V ternary nanowires (NWs) and heterostructures (HSs) of different types based on such NWs present an emerging class of nanomaterials that offer otherwise unattainable capabilities far beyond the 2D thin-film limit [1–6]. In particular, axial NW HSs BC/AC composed of lattice-mismatched III–V materials AC and BC can be grown without misfit dislocations if the NW radius is below the critical radius, which is typically in the order of a few tens of nanometers [7]. This property is due to the high surface-to-volume ratio of NWs allowing for the dislocation-free relaxation of elastic stress induced by lattice mismatch on the NW's sidewalls. For the same reason, NWs containing axial HSs can be grown without dislocations on Si substrates, offering a promising way for the monolithic integration of III–V photonics with the Si electronic platform [2,3]. III–V NW HSs are ideal for the generation of and manipulation with quantum light [8–10]. Most III–V NWs are fabricated through different epitaxy techniques using the vapor–liquid–solid (VLS) method with a foreign metal catalyst (often Au [11]), which can be replaced with a group III metal (Ga or In) in the self-catalyzed approach [12]. A detailed review of modeling approaches for the VLS growth of III–V NWs can be found, for example, in Ref. [13].

Compositions of VLS III–V ternary NWs based on a group V intermix and NW HSs based on a group V interchange were studied experimentally in different material sys-

tems, including InAsSb [14–18], GaAsSb [18–22], InAsP [23–29] and GaAsP [30–36]. It is generally believed that the interfaces of axial NW HSs based on the group V interchange should be sharper compared to group-III-based NW HSs of a similar radius [37–40], because the reservoir effect caused by the accumulation of different elements in a catalyst droplet [13,18,20,27,33,35–41] is largely reduced for highly volatile group V atoms. However, the measured compositional profiles were almost atomically sharp only for VLS InAs/InP/InAs [27] and GaAs/$GaAs_xP_{1-x}$/GaAs [36] double NW HSs, while the interfaces of VLS GaP/GaAs/GaP [33] and GaP/$GaAs_xP_{1-x}$/GaP [35] double NW heterostructures were comparable or even wider than in GaAs/$Al_xGa_{1-x}As$/GaAs NW HSs based on the group III interchange [39]. These examples showed that the compositional profiles across VLS axial NW HSs $A_{x_0}B_{1-x_0}C/A_{x_1}B_{1-x_1}C$ of a given radius are influenced by many factors, including the stationary compositions x_0 and x_1 and the crystallization rates of AC and BC pairs at the liquid–solid interface, rather than the total concentration of A and B atoms alone. The modeling strategies for the VLS growth of III–V ternary NWs and NW HSs are reviewed, for example, in Refs. [42] and [43]. In brief, they are based on the regular growth model [44], equilibrium [33,45] or nucleation-limited [46] and kinetic [47,48] models for the liquid–solid distribution $x(y)$ connecting the composition of $A_xB_{1-x}C$ NW with the relative fraction of atoms A in liquid y. The liquid composition y changes under time-dependent vapor fluxes of A and B atoms, producing a NW HS. With the known liquid–solid distribution $x(y)$, and using some assumptions on the axial growth rate of a HS, one can compute the compositional profile x versus the vertical distance ξ [45,46]. According to the current view [49,50], the liquid–solid distribution of VLS ternary III–V NWs is close-to-equilibrium in the case of the group III intermix and kinetic in the case of the group V intermix, because the liquid–solid growth always occurs under group-III-rich conditions. This property was indirectly used in Ref. [33] for modeling the compositional profiles in self-catalyzed GaAs/AlGaAs NW HSs. However, it was not implied in the existing models for group-V-based NW HSs [18,27,44,46].

The liquid–solid distribution of VLS III–V ternary NWs based on the group V intermix is reduced to the one-parametric Langmuir–McLean shape [51] at high enough supersaturations in liquid. This purely kinetic distribution depends solely on the ratio of the effective liquid–solid incorporation rates of AC and BC pairs [49,50], denoted as c_l in that which follows. The same Langmuir–McLean formula describes the equilibrium liquid–solid distribution for III–V ternaries with weak interactions between dissimilar pairs, such as AlGaAs, with a different parameter related to the ratio of the affinities of A and B atoms in liquid [39,45,46]. In Ref. [52], we presented the first attempt to develop a growth model for axial NW HSs based on the group V interchange, using a simplifying assumption on the time-independent total concentration of A and B atoms in liquid. Herein, we venture beyond this assumption and develop a self-consistent model for the compositional profiles across the axial NW HS $A_{x_0}B_{1-x_0}C/A_{x_1}B_{1-x_1}C$ with any stationary compositions x_0 and x_1. We use (i) quadratic dependences of the desorption rates of A_2 and B_2 dimers on the concentrations of A and B atoms in liquid [49–53] and (ii) linear dependences of the crystallization rates of AC and BC pairs at the liquid–solid interface on these concentrations [44]. The last assumption is a simplification of a complex growth process of a partial monolayer in VLS NWs [13], but should be valid for large enough droplets and high enough supersaturations in liquid. It yields the Langmuir–McLean shape of the liquid–solid distribution [44]. We explicitly calculate the time dependences of the concentrations of A and B atoms in liquid, the corresponding evolution of the droplet composition y and the NW composition x, the vertical coordinate ξ as a function of time and, finally, the compositional profile $x(\xi)$. The model contains a minimum number of four parameters and can be used for the compositional modeling of any III–V NW HS grown using different epitaxy techniques. It fits well the compositional data on GaP/$GaAs_xP_{1-x}$/GaP NW HSs [35] and forms a basis for further advancements in the field.

2. Model

We considered the VLS growth of the axial NW HS $A_{x_0}B_{1-x_0}C/A_{x_1}B_{1-x_1}C$, where A and B atoms belong to group V and C atoms belong to group III, with the stationary compositions x_0 and x_1. In particular, $x_0 = 0$ corresponds to the VLS growth of the ternary NW section $A_{x_1}B_{1-x_1}C$ on the binary stem BC, and $x_0 = 0$ and $x_1 = 1$ correspond to the NW HS BC/AC composed of pure binary compounds. The total numbers of A and B atoms in a liquid droplet, N_A and N_B, change in time according to:

$$\frac{dN_A}{dt} = V_A - V_A^{des} - K_A\chi_A,$$
$$\frac{dN_B}{dt} = V_B - V_B^{des} - K_B\chi_B \quad (1)$$

Here, V_i are the arrival rates into the droplet and V_i^{des} are the desorption rates from the droplet of atoms $i = A, B$. The terms $K_i\chi_i$ are the linear sinks due to the crystallization of AC and BC pairs at the liquid–solid interface under the droplet, with K_i as the corresponding crystallization or liquid–solid incorporation rates. The concentrations of $i = A, B$ atoms in liquid χ_i were defined according to the following:

$$\chi_A = \frac{N_A}{N_C + N_{Au} + N_A + N_B}, \quad \chi_B = \frac{N_B}{N_C + N_{Au} + N_A + N_B}, \quad (2)$$

where N_c and N_{Au} are the total numbers of group III atoms C and Au atoms in the droplet ($N_{Au} = 0$ for self-catalyzed VLS growth). Linear crystallization rates used in Equation (1) neglected the fractions of A and B atoms rejected by the growing island or partial monolayer, and, hence, contained no interactions of AC and BC pairs in solid. This is valid only when the diffusion fluxes into the island are much larger than the rejected fluxes, which requires high enough supersaturations of liquid with respect to the ternary solid [44,47–50]. In this case, Equation (1) should be valid for both self-catalyzed and Au-catalyzed VLS growths, because the regular growth rate of the partial monolayer of a ternary NW is limited by the incorporation of group V atoms at $\chi_i \ll \chi_C$ [49,50]. Due to $N_i \ll N_C + N_{Au}$ for highly volatile group V atoms A and B, we could use the following:

$$\chi_i = \frac{N_i}{N_{tot}}, \quad i = A, B, \quad N_{tot} \cong N_C + N_{Au} = \frac{\pi R^3 f(\beta)}{3\Omega_L} \cong \text{const}. \quad (3)$$

The total number of atoms in the droplet $N_{tot} \cong N_C + N_{Au}$ is related to the radius of the NW top R and the contact angle of the droplet β, with Ω_L as the elementary volume per atom in liquid and $f(\beta)$ as the known geometrical function of the droplet contact angle β [13].

The desorption rates V_i^{des} of group V elements in the form of dimers A_2 and B_2 had to be proportional to χ_i^2 and to the droplet surface area [13,49,50,52,53]. The surface diffusion of group V adatoms is usually negligible [53]. Therefore, we could write the following:

$$V_i = \frac{h}{\Omega_S}\sigma_i v_i \frac{2\pi R^2}{1+\cos\beta}, \quad V_i^{des} = \frac{h}{\Omega_S}\sigma_i v_i^{des} \frac{2\pi R^2}{1+\cos\beta}\chi_i^2, \quad i = A, B. \quad (4)$$

Here, h is the height of a NW monolayer, Ω_S is the elementary volume per III–V pair in solid, v_i are the deposition rates of group V atoms ($v_i = 2v_{i_2}$ for the deposition of dimers A_2 and B_2), v_i^{des} are the known desorption factors ($v_i = 2v_{i_2}^{dea}$) which can be found, for example, in Refs. [49,50,52,53], and σ_i are the effective condensation coefficients or incorporation probabilities of group V species at the liquid surface [24,49,50,52]. The axial growth rate of a ternary NW, $d\xi/dt$, where ξ is the vertical distance in monolayers, is related to the sum of the two crystallization rates according to the following:

$$\frac{\pi R^2 h}{\Omega_S}\frac{d\xi}{dt} = K_A\chi_A + K_B\chi_B \quad (5)$$

Using Equations (3) to (5) in Equation (1), the governing equations describing the VLS growth and time-dependent composition of a ternary NW could be presented in the form shown below:

$$\frac{d\chi_i}{dt} = \gamma\left(\Phi_i - \Phi_i^{des}\chi_i^2 - g_i\chi_i\right), \quad i = A, B, \quad (6)$$

$$\frac{d\xi}{dt} = g_A\chi_A + g_B\chi_B. \quad (7)$$

The parameters were given as follows:

$$\Phi_i = \frac{2\sigma_i}{1+\cos\beta}v_i, \quad \Phi_i^{des} = \frac{2\sigma_i}{1+\cos\beta}v_i^{des}, \quad g_i = \frac{\Omega_S}{\pi R^2 h}K_i, \quad (8)$$

and

$$\gamma = \frac{3\Omega_L h}{\Omega_S R f(\beta)}. \quad (9)$$

Clearly, Φ_i and $\Phi_i^{des}\chi_i^2$ stand for the direct impingement and desorption of group V species, respectively, while $g_i\chi_i$ describe the regular crystallization of AC and BC pairs producing a ternary solid. The sum of the two crystallization rates determines the vertical growth rate of a NW. With the known fluxes Φ_i, our model contained only four control parameters, Φ_A^{des}, Φ_B^{des}, g_A and g_B, describing the desorption rates of the A_2 and B_2 dimers and the crystallization rates of the AC and BC pairs at the growth interface, respectively, as shown in Figure 1. The desorption rates are the known functions of temperature and can be calculated for any III–V ternary [49,50,52,53]. However, the crystallization rates g_i contain the generally unknown diffusion coefficients of A and B atoms in a quaternary liquid [49,50] and their values can be estimated only by fitting the experimental data on the interfacial profiles across NW HSs.

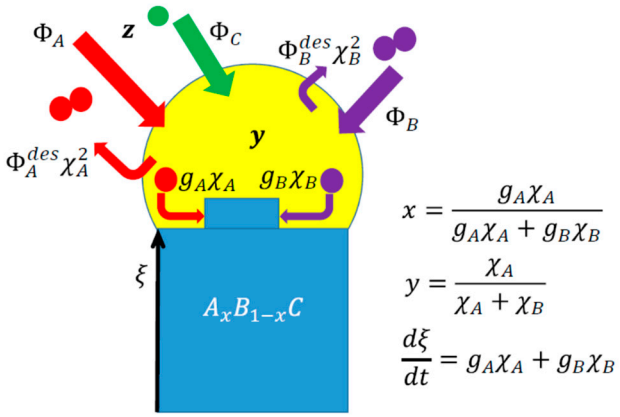

Figure 1. Illustration of the model parameters for VLS growth of III–V ternary NW HS based on group V intermix from vapor fluxes Φ_A, Φ_B and Φ_c. The desorption rates of group V dimers $\Phi_i^{des}\chi_i^2$ are proportional to the squared concentrations of group V atoms in liquid. The crystallization rates of dissimilar III–V pairs $g_i\chi_i$ scale linearly with χ_i. The vapor composition z is determined by the fluxes. The solid composition x is given by the ratio of the crystallization rate of AC pairs over the total crystallization rate, which equals the axial NW growth rate $d\xi/dt$.

We noted that the regular growth rates K_i were proportional to πR^2, hence, g_i were independent of R [44]. The geometrical parameter γ was the same as in Refs. [27,39,44–46,52]. It decreased for larger R and β, showing that the strength of the reservoir effect increased for larger droplets. By solving Equation (6) after the group V flux commutation and using

the boundary conditions before the commutation, we obtained the concentrations of A and B atoms χ_A and χ_B in liquid versus time. This gave the following liquid composition:

$$y = \frac{\chi_A}{\chi_A + \chi_B} \tag{10}$$

as a function of time. The solid composition in our model was obtained through the Langmuir–McLean formula:

$$x = \frac{g_A\chi_A}{g_A\chi_A + g_B\chi_B} = \frac{c_l y}{1 + (c_l - 1)y}, \; c_l = \frac{g_A}{g_B} = \frac{K_A}{K_B}, \tag{11}$$

and was obtained at the known y as a function of time. Finally, the interfacial profile $\xi(t)$ was calculated through the integration of Equation (7) with the obtained time-dependences $\chi_A(t)$ and $\chi_B(t)$, which yielded the compositional profile $x(\xi)$ versus the vertical coordinate.

Let us now discuss the novelty of the model with respect to the previous works. A similar growth model was earlier considered in Ref. [44]. However, it was not suited for ternaries based on the group V intermix because the desorption terms were assumed linear in χ_i. The model of Ref. [27] entirely neglected the sinks of group V atoms through crystallization, assuming that the desorption fluxes of A and B atoms were much larger than the crystallization rates of AC and BC pairs, which is not true in the general case. The models of Refs. [39,45,46] and their generalizations [43] did not consider any desorption and, hence, were valid for HW HSs based on the group III interchange. The model of Ref. [52] used the assumption $g_A\chi_A + g_B\chi_B = \Phi_A - \Phi_A^{des}\chi_A^2 + \Phi_B - \Phi_B^{des}\chi_B^2$; hence, $g_A\chi_A = x(\Phi_A - \Phi_A^{des}\chi_A^2 + \Phi_B - \Phi_B^{des}\chi_B^2)$ and $g_B\chi_B = (1-x)(\Phi_A - \Phi_A^{des}\chi_A^2 + \Phi_B - \Phi_B^{des}\chi_B^2)$. This eliminated the crystallization rates $g_A\chi_A$ and $g_B\chi_B$ from the model and yielded $\chi_A + \chi_B =$ const at any time. Obviously, the condition of a time-independent total concentration of group V atoms in liquid could be broken in non-stationary regime of VLS growth under varying material fluxes. One could also use the approximation $g_A\chi_A + g_B\chi_B = \Phi_C$ in group-III-limited VLS growth of Au-catalyzed NWs [13,54] or under close-to-equilibrium conditions at a time-independent droplet volume [49,50]. The total flux of group III atoms Φ_C included their surface diffusion [13,49,50,54–57]. Our model was more general, because it considered the binary crystallization rates independently of the deposition and desorption fluxes and allowed for the accumulation or depletion of group V atoms in the droplet beyond the approximation of $\chi_A + \chi_B =$ const.

3. Stationary State

- Stationary solutions to Equation (6) were given as follows:

$$\chi_i^s = \frac{\sqrt{1 + 4\varphi_i\psi_i} - 1}{2\psi_i},$$
$$\varphi_i = \frac{\Phi_i}{g_i}, \; \psi_i = \frac{\Phi_i^{des}}{g_i}. \tag{12}$$

When $\varphi_i\psi_i = \Phi_i\Phi_i^{des}/g_i^2 \ll 1$, we simply had $\chi_i^s \cong \Phi_i/g_i$, that is, the stationary concentrations were proportional to the vapor fluxes of group V atoms. This corresponded to low desorption rates at a growth temperature or low deposition rates relative to the binary crystallization rates g_i. In the opposite case of $\Phi_i\Phi_i^{des}/g_i^2 \gg 1$, corresponding to the desorption-limited VLS growth, the stationary concentrations $\chi_i^s \cong \sqrt{\Phi_i/\Phi_i^{des}}$ were independent of g_i. In our model, the low stability of group V atoms in the droplet ($\chi_i^s \ll 1$) could be due not only to the high desorption rates at elevated temperatures (large $\Phi_i^{des} \gg \Phi_i$), but also to high crystallization rates (large $g_i \gg \Phi_i$) even in the regimes with a low desorption.

The stationary solutions given by Equation (12) together with Equations (10) and (11) yielded the vapor–solid distribution $x_s(z)$ connecting the NW composition x with the

fraction of A atoms in vapor z. Let us consider the VLS growth of a ternary NW from the vapor fluxes:

$$\Phi_A = \sigma_A \Phi_{tot} z,\ \Phi_B = \sigma_B \Phi_{tot}(1-z),\ \Phi_{tot} = \frac{2}{1+\cos\beta} v_{tot}, \quad (13)$$

where $v_{tot} = v_A + v_B$ is the total deposition rate of group V atoms A and B. Using this in Equations (10) to (12), we obtained the following:

$$x_s = \frac{1}{1+G_s},\ G_s = u\frac{\sqrt{1+4\frac{\Gamma_A(1-z)}{c_g u}}-1}{\sqrt{1+4\Gamma_A z}-1}, \quad (14)$$

with the below parameters:

$$\Gamma_A = \frac{\sigma_A \Phi_{tot} \Phi_A^{des}}{g_A^2}, u = \frac{\Phi_A^{des}}{\Phi_B^{des}} \frac{1}{c_l^2},\ c_g = \frac{\sigma_A}{\sigma_B}. \quad (15)$$

Here, the parameter Γ_A is similar to $\Phi_A \Phi_A^{des}/g_A^2$, and describes the fraction of desorbed atoms A. The parameter u accounts for the difference in the desorption rates of atoms A and B and the incorporation rates of AC and BC pairs at the liquid–solid interface. The parameter c_g is related to the possible difference in the incorporation of atoms A and B at the droplet surface [24,30,49,50,52,55]. The vapor–solid distribution given by Equation (14) was simplified, because it neglected the interactions in a solid and contained no miscibility gaps for systems with strong interactions between dissimilar III–V pairs [50]. However, it described the transformation from the Langmuir–McLean kinetic shape (which became $x = z$ at $c_g = 1$) at low deposition rates of group V atoms or V/III ratios to a non-linear shape at high deposition rates or V/III ratios, caused by the enhanced desorption of the excessive group V species [14,49,50]. Indeed, at $\Gamma_A \to 0$, we had $G_s \to (1-z)/(c_g z)$, which gave the following Langmuir–McLean vapor–solid distribution:

$$x_s = \frac{c_g z}{1+(c_g-1)z}. \quad (16)$$

In the regime with high desorption of both group V elements at $\Gamma_A \to \infty$, $G_s \to (u/c_g)^{1/2}[(1-z)/z]^{1/2}$ and the vapor–solid distribution became the following:

$$x_s = \frac{\sqrt{z}}{\sqrt{z}+v\sqrt{1-z}}, v = \sqrt{u/c_g}. \quad (17)$$

If atoms A incorporated into the liquid–solid interface much faster than atoms B, we could use $u \to \infty$ at $c_l^2 \to 0$, in which case $G_s \to (2\Gamma_A/c_g)(1-z)/(\sqrt{1+4\Gamma_A z}-1)$. In any case, the vapor–solid distribution became more non-linear in the regimes with an enhanced desorption of at least one group V element.

Figure 2 shows the measured vapor–solid distributions of $GaAs_xP_{1-x}$ NWs grown with Ga-catalyzed molecular beam epitaxy (MBE) at 630 °C under high V/III flux ratios > 16, as shown in Refs. [35] and [30]. The experimental curves were quite similar and demonstrated the difficult incorporation of As atoms into GaAsP in comparison to P atoms. Unfortunately, these limited datasets could be equally well-fitted using different expressions. The Langmuir–McLean fits required small values of $c_g = 0.247$ and 0.335 to describe the lower As incorporation rate. The fits using Equation (14) required $u \to \infty$, suggesting that $c_l \ll 1$, which corresponded to a much faster transfer of P atoms from liquid to solid relative to As atoms. The large fitting values of $\Gamma_A = 20$ and 9.5 suggested that most As atoms desorbed from the droplet. Therefore, it could not be stated which stationary state was closer to reality. More growth experiments with different III–V–V ternary NWs under different conditions (temperature, total V/III flux ratio, growth cat-

alyst, etc.) are required for the accurate identification of the key factors influencing the shape of the vapor–solid distributions [49,50]. We noted, however, that the incomplete adsorption of As_2 dimers on the liquid Ga surface in MBE was unlikely, and that the Langmuir–McLean curves with $c_g < 1$ should not have corresponded to the negligible desorption of As and P species from liquid. The desorption of both As_2 and P_2 dimers from the droplet surface should have been significant at a high growth temperature of 630 °C [13,50,53]. Rather, the low-fitting values of c_g in the Langmuir–McLean formula described in a qualitative way a larger fraction of desorbed As atoms in the Ga-catalyzed VLS growth of GaAsP NWs. This conclusion was earlier discussed in Ref. [50] in connection with the Langmuir–McLean fits of the stationary vapor–solid distributions of Ga-catalyzed GaAsP [30,32,35], Au-catalyzed GaAsP [58] and Au-catalyzed InAsP [24] VLS NWs grown at different temperatures through different epitaxy techniques. Furthermore, the Langmuir–McLean vapor–solid distributions were previously used for fitting the compositional data on GaAsP epilayers [59]. In GaAsP and InAsP material systems, the pseudo-binary interaction constants between IIIAs and IIIP pairs ω were noticeably lower than the critical value of 2 (in thermal units). For example, $\omega = 0.641$ for GaAsP at 630 °C [60]. Consequently, the exponential terms describing interactions in solid were weak and had little influence on the shape of the vapor–solid distributions [50]. This additional factor improved the correspondence of the Langmuir–McLean fits with the data on GaAsP and InAsP ternaries, even when the growth conditions were close-to-equilibrium [50].

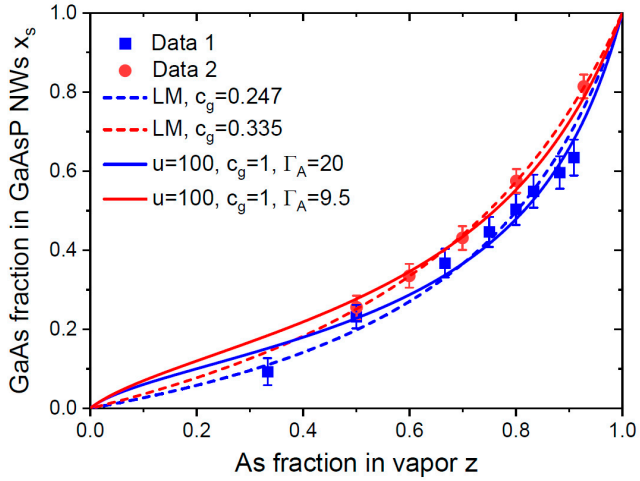

Figure 2. Stationary vapor–solid distributions of GaAsP NWs grown using Ga-catalyzed MBE at 630 °C in Ref. [35] (Data 1) and [30] (Data 2) (symbols), fitted using the Langmuir–McLean (LM) formula given through Equation (16) with c_g given in the legend (dashed lines) and Equation (14) at $c_g = 1$ and other parameters given in the legend (solid lines).

4. Compositional Profiles

We now considered the time-dependent concentrations $\chi_i(t)$ under the varying vapor fluxes of A and B species. The most general case corresponded to a NW heterostructure $A_{x_0}B_{1-x_0}C/A_{x_1}B_{1-x_1}C$, with the two stationary compositions $x_s = x_0$ and x_1, stationary concentrations $\chi_i^s = \chi_i^0$ and χ_i^1, obtained under the material fluxes $\Phi_A^0 = \sigma_A\Phi_{tot}^0 z_0$, $\Phi_B^0 = \sigma_B\Phi_{tot}^0(1-z_0)$, $\Phi_A^1 = \sigma_A\Phi_{tot}^1 z_1$ and $\Phi_B^1 = \sigma_B\Phi_{tot}^1(1-z_1)$. The stationary concentrations $\chi_i^s = \chi_i^0$ and χ_i^1 were given using Equation (12) with these vapor fluxes. Exact solutions to Equation (6) with the initial conditions $\chi_i(t = t_0) = \chi_i^0$ were obtained with the below equations:

$$\chi_i(t) = \chi_i^1 + \frac{2(\chi_i^0 - \chi_i^1)}{(1+\varepsilon_i)\exp\left(\frac{t-t_0}{\tau_i}\right) + 1 - \varepsilon_i}, \; i = A, B, \tag{18}$$

with the following parameters:

$$\varepsilon_i = \frac{1+2\psi_i\chi_i^0}{1+2\psi_i\chi_i^1} = \sqrt{\frac{1+4\varphi_i^0\psi_i}{1+4\varphi_i^1\psi_i}}, \quad \frac{1}{\tau_i} = \gamma g_i\left(1+2\psi_i\chi_i^1\right). \tag{19}$$

The fraction of atoms A in liquid versus time was obtained from Equation (10). The solid composition versus time was obtained from Equation (11), which could equivalently be written as follows:

$$x(t) = \frac{1}{1+G(t)}, \; G(t) = \frac{g_B\chi_B(t)}{g_A\chi_A(t)} = \frac{1}{c_l}\frac{\chi_B(t)}{\chi_A(t)}. \tag{20}$$

This gave the full picture of the VLS growth process and the droplet/NW composition as a function of time. Then, using Equation (18) in Equation (7) and integrating it with the initial condition $\xi(t=t_0)=\xi_0$, we obtained the vertical coordinate as a function of time:

$$\xi(t) - \xi_0 = F_A(t) + F_B(t),$$

$$F_i(t) = g_i\chi_i^1(t-t_0) - \frac{g_i\left(\chi_i^0-\chi_i^1\right)}{1-\varepsilon_i}\tau_i \ln\left\{\frac{1+\varepsilon_i+(1-\varepsilon_i)\exp\left[-\frac{(t-t_0)}{\tau_i}\right]}{2}\right\}, \; i = A, B. \tag{21}$$

Equations (20) and (21) gave the compositional profile across the NW HS in the form of the implicit function, but not explicitly.

In the absence of the vapor flux of $i = A$ or B atoms ($\Phi_i = \varphi_i = 0$, $\chi_i^1 = 0$), Equation (18) was reduced to as shown:

$$\chi_i = \frac{\chi_i^0}{\left(1+\psi_i\chi_i^0\right)e^{\gamma g_i(t-t_0)} - \psi_i\chi_i^0} \tag{22}$$

This corresponded to the decrease in the concentration of $i = A$ or B atoms from χ_i^0 to zero after turning off their input. The depletion occurred due to the desorption of the residual atoms to vapor and their incorporation into solid. In the regime with negligible desorption ($\psi_i \to 0$), the droplet was depleted only due to the crystallization of AC or BC pairs:

$$\chi_i = \chi_i^0 e^{-\gamma g_i(t-t_0)}. \tag{23}$$

In the absence of the desorption of the group V element i ($\psi_i \to 0$, $\varepsilon_i \to 1$), the function $G(t)$ in Equation (20) was simplified to the below:

$$G = \frac{\Phi_B^1 + \left(\Phi_B^0 - \Phi_B^1\right)e^{-\gamma g_B(t-t_0)}}{\Phi_A^1 + \left(\Phi_A^0 - \Phi_A^1\right)e^{-\gamma g_A(t-t_0)}}. \tag{24}$$

The vertical coordinate ξ became the following:

$$\xi(t) = \xi_0 + \left(\Phi_A^1 + \Phi_B^1\right)(t-t_0) + \frac{\left(\Phi_A^0 - \Phi_A^1\right)}{\gamma g_A}\left[1 - e^{-\gamma g_A(t-t_0)}\right] + \frac{\left(\Phi_B^0 - \Phi_B^1\right)}{\gamma g_B}\left[1 - e^{-\gamma g_B(t-t_0)}\right]. \tag{25}$$

These equations contained only the vapor fluxes Φ_i^0 and Φ_i^1 before and after the group V flux commutation. The concentrations of atoms A and B in liquid were given using $\chi_i^0 = \Phi_i^0/g_{\copyright}$ and $\chi_i^1 = \Phi_i^1/g_i$.

Figure 3 show the solutions obtained from Equations (20), (24) and (25) without the desorption of both group V elements from the droplet. The coefficient in the Langmuir–McLean vapor–solid distribution c_g was set to 0.247, as in Figure 2, for the data of Ref. [35]. The parameter γ was set to 0.000758, which corresponded, for example, to a 110 nm radius GaAsP NW with $\beta = 120°$ [52]. We used the total fluxes such that $2/(1+\cos\beta)]\sigma_B v_{tot}^0 = [2/(1+\cos\beta)]\sigma_B v_{tot}^1 = 1$ ML/s. At $z_0 = 0$, $z_1 = 0.5$, the input fluxes were given as fol-

lows: $\Phi_A^0 = 0$, $\Phi_B^0 = 1$ ML/s and $\Phi_A^1 = 0.1235$ ML/s, $\Phi_B^1 = 0.5$ ML/s. At $z_0 = 0.5$ and $z_1 = 1$. The input fluxes were given as follows: $\Phi_A^0 = 0.1235$ ML/s, $\Phi_B^0 = 0.5$ ML/s and $\Phi_A^1 = 0.247$ ML/s and $\Phi_B^1 = 0$. We chose $g_B = 100$ ML/s, corresponding to $\chi_B^0 = \Phi_B^0/g_B = 0.01$ at $z_0 = 0$. Three different $c_l = 0.1$, 1 and 10 then yielded $g_A = 10$, 100 and 1000 ML/s and $\chi_A^1 = \Phi_A^1/g_A = 0.0247$, 0.00247 and 0.000247, respectively, at $z_1 = 0.5$. Figure 3a,b show that both x and y became more abrupt functions of time for larger c_l. The time-dependent profiles were largely influenced by the initial NW composition x_0, which equaled zero at $z_0 = 0$ and 0.2 at $z_0 = 0.5$. At a small c_l of 0.1, the $x(t)$ dependence in the direct transition was much sharper if we started from a non-zero x_0. For example, As atoms were more stable in liquid compared to P atoms [27,52], corresponding to $c_l < 1$, or even $c_l \ll 1$, for $GaAs_xP_{1-x}$ NWs. This explained why the $GaAs_xP_{1-x}/GaAs/GaAs_xP_{1-x}$ interfaces of Ref. [36] were much sharper than the $GaP/GaAs_xP_{1-x}/GaP$ interfaces of Ref. [35], even if they were grown in the self-catalyzed VLS mode under very similar MBE conditions and temperatures (630 °C in Ref. [35] and 640 °C in Ref. [36]). This important observation was recognized in Ref. [52] using a different model. The effect remained if the desorption of As and P atoms was included (see Figure 3 below). According to Figure 3c, the vertical distance versus time was composed of two almost linear segments, with the abrupt change in the slope angle at the flux commutation. This corresponded to higher growth rates of NW sections with smaller fractions x of AC material in the ternary $A_xB_{1-x}C$ NW. Smaller x were obtained at lower z, which yielded higher total fluxes of group V atoms due to $c_g < 1$ with our parameters. The growth rates of NW HSs at $z_0 = 0$, $z_1 = 0.5$ were, therefore, much higher than at $z_0 = 0.5$, $z_1 = 1$. This property strongly affected the compositional profiles $x(\xi)$ in Figure 3d, which became significantly thinner for lower growth rates at larger z. Otherwise, the shapes of the compositional profiles $x(\xi)$ in Figure 3d were quite similar to the $x(t)$ dependences in Figure 3a. In particular, we obtained broader heterointerfaces at a small c_l of 0.1 and $z_0 = 0$, that is, when the NW HSs started from a pure BC segment. At $z_0 = 0.5$, the interfacial abruptness at $c_l = 0.1$ largely improved, particularly for the direct transition. The interfaces at $c_l = 1$ and 10 became almost indistinguishable.

Figure 4 shows the same dependences obtained from Equations (18) to (21), where the desorption of A and B species was included. In this case, we used $c_g = 1$, corresponding to the 100% incorporation of both A_2 and B_2 dimers from vapor into the droplet. The parameter γ equaled 0.000758, as in Figure 3. The parameter c_l equaled 0.1, meaning that atoms A were more stable in the droplet than atoms B as for As and P atoms in the Ga-catalyzed growth of $GaAs_xP_{1-x}$ NWs [35,36]). We assumed that $\Phi_A^{des} = \Phi_B^{des}$. The total input fluxes of group V atoms were fixed at $\sigma_A\Phi_{tot}^0 = \sigma_B\Phi_{tot}^0 = \sigma_A\Phi_{tot}^1 = \sigma_B\Phi_{tot}^1 = 1$ ML/s. At $z_0 = 0$, $z_1 = 0.5$, the vapor fluxes of A and B atoms were given as follows: $\Phi_A^0 = 0$, $\Phi_B^0 = 1$ ML/s and $\Phi_A^1 = 0.5$ ML/s, $\Phi_B^1 = 0.5$ ML/s. At $z_0 = 0.5$, $z_1 = 1$, the fluxes were given as follows: $\Phi_A^0 = 0.5$ ML/s, $\Phi_B^0 = 0.5$ ML/s and $\Phi_A^1 = 1$ ML/s, $\Phi_B^1 = 0$. We chose $g_B = 100$ ML/s and, hence, $g_A = c_l g_B = 10$ ML/s. Three different $\Gamma_A = 1$, 5 and 20 yielded $\Phi_A^{des} = \Phi_B^{des} = 100$, 500 and 2000 ML/s, respectively. The stationary concentrations of group V atoms in liquid at different transitions are given in Table 1. A larger Γ_A corresponded to higher desorption rates of both A_2 and B_2 dimers from the droplet, which was why their concentrations decreased with Γ_A. The concentrations of B atoms were much lower than for A atoms in all cases due to a small c_l of 0.1. At the same desorption coefficients ($\Phi_A^{des} = \Phi_B^{des}$), lower concentrations of B atoms were explained solely by their faster transfer from liquid to solid. The general trend of sharpening the NW HSs by using the ternary NW stem $A_{x_0}B_{1-x_0}C$ with $x_0 = 0.2 - 0.45$ for growing a pure AC segment on its top remained the same as in Figure 3.

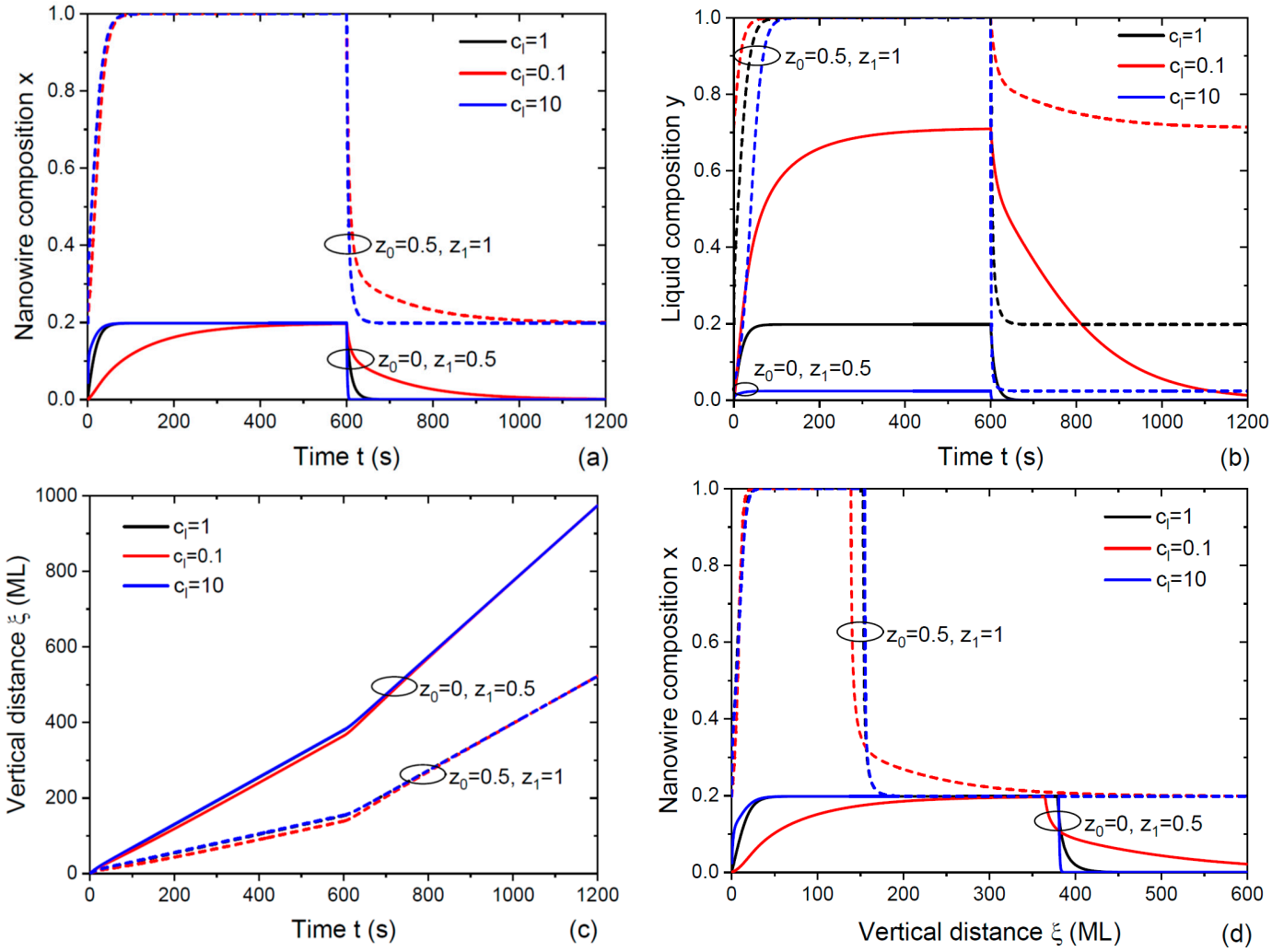

Figure 3. (**a**) Time-dependent NW composition, (**b**) liquid composition, (**c**) vertical distance and (**d**) coordinate-dependent compositional profiles across double NW HSs with different stationary fractions of group V atoms A in vapor: $z_0 = 0$, $z_1 = 0.5$ (solid lines) and $z_0 = 0.5$, $z_1 = 1$ (dashed lines). The curves were obtained from Equations (20), (24) and (25) without desorption at $c_g = 0.247$, $\gamma = 0.000758$ and three different $c_l = 1$, 0.1 and 10. Other parameters are given in the main text.

Table 1. Stationary concentrations of A and B atoms for NW HSs shown in Figure 4.

	Γ_A	1	5	20
$z_0 = 0$ $z_1 = 0.5$	χ_A^0	0	0	0
	χ_A^1	0.0366	0.0232	0.0135
	χ_B^0	0.0099	0.00954	0.00854
	χ_B^1	0.00498	0.00488	0.00458
$z_0 = 0.5$ $z_1 = 1$	χ_A^0	0.0366	0.0232	0.0135
	χ_A^1	0.0618	0.0358	0.020
	χ_B^0	0.00498	0.00488	0.00458
	χ_B^1	0	0	0

The NW HSs in Figure 4 became thinner for higher desorption rates. Enhanced desorption improved the interfacial abruptness, as clearly seen from Figure 4d. This important conclusion could be understood as follows: The reservoir effect, caused by the

accumulation of, for example, atoms B, in a catalyst droplet when growing a pure AC NW segment [13,18,20,27,33,35–41,52] contributed to the interfacial broadening only through the crystallization of a BC pair together with AC pairs at the liquid–solid interface. In the VLS growth regimes with low desorption, almost all atoms B would be transferred from liquid to solid, while most of these atoms would evaporate without influencing the interfacial abruptness when their desorption was enhanced. Similar considerations were used in Ref. [33] for sharpening the self-catalyzed GaAs/GaP NW HSs by switching all material fluxes for a short time at the group V flux commutation.

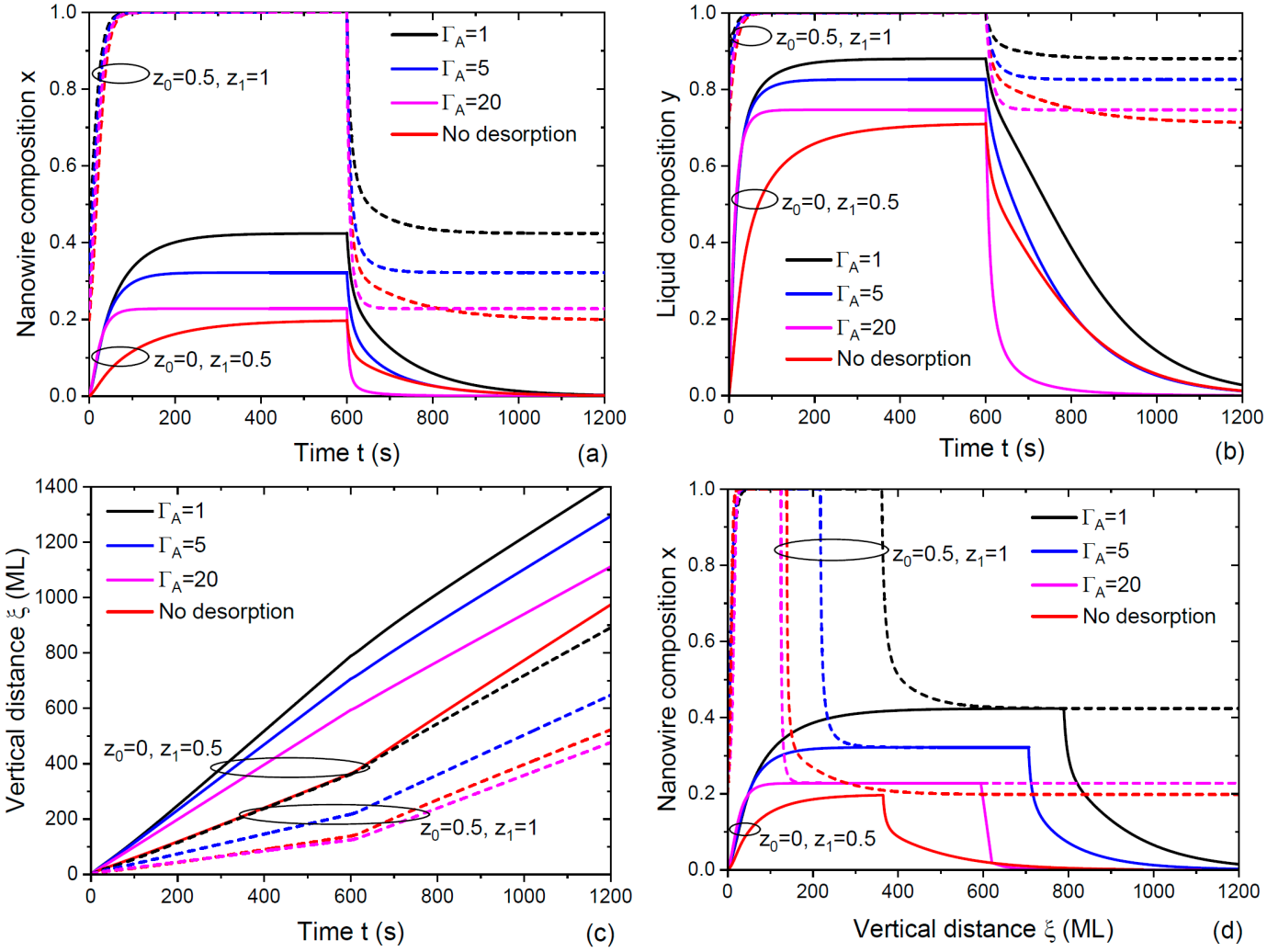

Figure 4. Same as Figure 3 with the desorption of A_2 and B_2 dimers from the droplet: (**a**) Time-dependent NW composition, (**b**) liquid composition, (**c**) vertical distance and (**d**) coordinate-dependent compositional profiles across double NW HSs. The curves were obtained from Equations (18) to (21) at $c_g = 1$ (equivalent incorporation of A and B species into the droplet), $c_l = 0.1$ (high stability of A atoms in liquid relative to B atoms), $\gamma = 0.000758$ and three different $\Gamma_A = 1$, 5 and 20. Larger Γ_A corresponded to higher desorption rates of both group V elements. Other parameters are given in the main text and in Table 1. The curves without desorption at $c_g = 0.247$ and $c_l = 0.1$ from Figure 3 were included for comparison.

To demonstrate the effect more clearly, we noted that the $\xi(t)$ curves in Figures 3c and 4c were almost linear, with the axial growth rate changing very abruptly upon the flux commutation. In this case, we could use the approximation of a time-independent axial growth rate of a NW HS at a given transition:

$$v = g_A\chi_A + g_B\chi_B \cong \text{const} \quad (26)$$

Equations (11) and (7) were then reduced to $x \cong g_A \chi_A / v$ and $\xi - \xi_0 \cong v(t - t_0)$. Using this in Equation (18), we obtained the simplified expression for the compositional profile:

$$x \cong x_1 + \frac{2(x_0 - x_1)}{(1+\varepsilon)\exp\left(\frac{\xi-\xi_0}{\Delta\xi}\right) + 1 - \varepsilon},$$

$$\varepsilon = \frac{1+2\omega x_0}{1+2\omega x_1}, \quad \Delta\xi = \frac{v}{\gamma g_A (1+2\omega x_1)}, \quad \omega = \frac{\psi_A v}{g_A} = \frac{\Phi_A^{des} v}{g_A^2}. \tag{27}$$

This formula contained the experimentally measurable stationary compositions x_0 and x_1; the axial growth rates v could also be measured for each transition [27,33,35,36]. The parameter γ given by Equation (9) was known from the NW geometry (R and β). The crystallization rate of AC pairs g_A and, hence, ω, were generally unknown, because g_A contained the unknown diffusion coefficient of atoms A in Ga or Ga–Au liquid [50]. However, the characteristic interfacial abruptness $\Delta\xi$ could be estimated from fitting the experimental compositional profiles for a given material system. From Equation (27), the interfacial abruptness at a given $v/\gamma g_A$ improved for larger ω, and ω increased for a higher desorption rate Φ_A^{des}. Figure 5 shows that the double NW HS with $x_0 = 0$ and $x_1 = 0.5$ became sharper when desorption was enhanced, particularly at the direct transition.

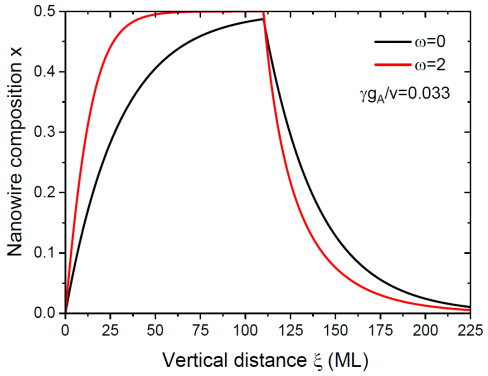

Figure 5. Compositional profiles across double NW HS $BC/A_{0.5}B_{0.5}C/BC$ without ($\omega = 0$) and with ($\omega = 2$) desorption of group V elements, obtained from Equation (27) at a fixed $\gamma g_A / v$ of 0.033, corresponding to the same axial growth rate at both transitions.

5. Theory and Experiment

Figure 6a shows the measured compositional profiles in double NW HSs $GaP/GaAs_{x_1}P_{1-x_1}/GaP$ with different stationary compositions x_1 from 0.093 to 0.65, as shown in Figure 1 (Data 1 from Ref. [35]). The NW HSs were grown using Ga-catalyzed MBE at 630 °C on Si(111) substrates. The Ga deposition rate was fixed in all experiments. GaP NW stems as well as pure GaP sections in the NW HSs were grown at a V/III flux ratio of eight, which gave an average axial growth rate of 1.362 ML/s. Different fractions of GaAs in ternary GaAsP sections were achieved by changing the As/P flux ratio from 0.5 to 10. The total V/III flux ratio was kept at 16 for As/P ratios from 0.5 to 2, and at 32 for As/P ratios larger than 2. The average radius of the NW HSs was 110 nm, and the contact angle was estimated at 120° in Ref. [52], yielding $\gamma = 0.000758$ from Equation (9). The dashed lines in Figure 6a show the best fits obtained from our model without desorption. These curves were calculated using Equations (20), (24) and (25), where we took into account the increase in the total flux of group V atoms from 1.362 ML/s for pure GaP to 2.724 for $GaAs_{x_0}P_{1-x_0}$ with low $x_1 \leq 0.367$ at As/P ratios ≤ 2 and to 5.448 for higher x_1 at larger As/P ratios. The parameter c_g was fixed at 0.247, according to the best fit obtained through the Langmuir–McLean vapor–solid distribution in Figure 1. Other parameters are summarized in Table 2. Figure 6b shows the vertical distance ξ versus time, obtained with these parameters and used in calculations of the compositional profiles. We noted that the growth

time of the GaAsP segments was 36 s and 18 s for As/P ratios ≤ 2 and > 2, respectively [35]. The model without desorption required a low $c_g = 0.247$ to fit the stationary vapor–solid distributions in Figure 2. Therefore, the increase in the As flux with respect to the P flux did not produce the required increase in the axial growth rate, according to Figure 6b.

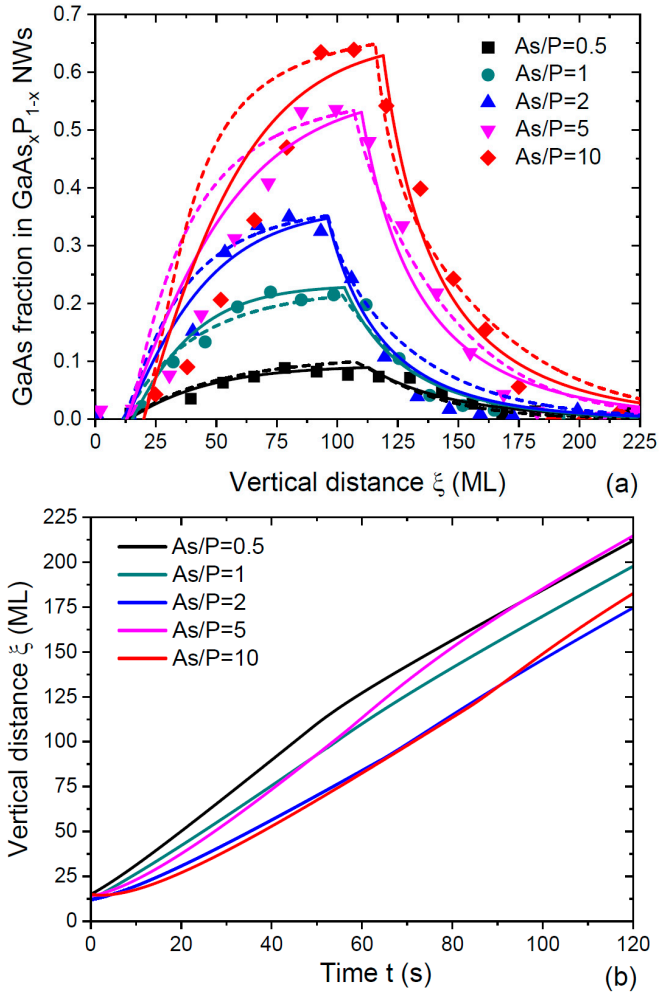

Figure 6. (**a**) Compositional profiles across double NW HSs GaP/$GaAs_{x_1}P_{1-x_1}$/GaP with different stationary compositions x_1, grown using Ga-catalyzed MBE at 630 °C under different As/P ratios, as shown in the legend [35] (symbols). Dashed lines show the fits obtained from the model without desorption at $c_g = 0.247$ and $\gamma = 0.000758$, with other parameters summarized in Table 2. Solid lines show the fits obtained from the model with desorption at $c_g = 1$ and $\gamma = 0.000758$, with other parameters summarized in Table 3. (**b**) Vertical distance versus time at different As/P ratios used in calculations of the compositional profiles without desorption in (**a**).

As mentioned above, the desorption of As_2 and P_2 dimers from the Ga droplet should have been significant at 630 °C. The solid lines in Figure 6a show the best fits obtained from Equations (27) with desorption at $c_g = 1$ and the same γ of 0.000758. In these fits, the axial growth rate v was calculated as the linear interpolation of the HS height with the known growth times (36 and 18 s). The fitting parameters are summarized in Table 3. The use of the general model given by Equations (18) to (21) resulted in almost identical curves. It could be seen that the calculated compositional profiles were narrower in the model with desorption. Figure 7 shows the comparison of the fits to the data of Ref. [35] obtained in Ref. [52] and using our model with desorption. Additionally, we showed the fits to the data of Ref. [36], where pure GaAs segments were grown on ternary $GaAs_{0.6}P_{0.4}$ stems through Ga-catalyzed MBE at 640 °C under conditions similar to Ref. [35]. Pure GaAs segments were achieved through the termination of the P flux ($x_1 = 1$). These NWs had a uniform

radius of 30 nm, and the contact angle estimated in Ref. [52] was approximately 135°. The corresponding value of γ equaled 0.00135, according to Equation (9). The Ga droplets on top of these NWs were smaller than in Ref. [35]. Consequently, the characteristic interfacial abruptness $\Delta\xi_c = v/\gamma g_A$ decreased from ~40 MLs (see the fitting parameters for the data of Ref. [35] in Table 3) to 25 MLs for Ref. [36]. The fitting value of $\omega = 2$ was the same for the data of Refs. [35] and [36]. This seemed plausible, because both GaAsP NW HSs were grown using Ga-catalyzed MBE at similar temperatures of 630–640 °C.

Table 2. Fitting parameters for GaP/$GaAs_xP_{1-x}$/GaP NW HSs in Figure 6 without desorption.

Direct Transition from GaP to $GaAs_xP_{1-x}$					
As/P flux ratio	0.5	1	2	5	10
z	0.333	0.5	0.667	0.833	0.909
Φ^1_{tot} (ML/s)	2.724	2.724	2.724	5.448	5.448
Φ^0_P (ML/s)	1.362	1.362	1.362	1.362	1.362
Φ^0_{As} (ML/s)	0	0	0	0	0
$\Phi^1_{As} + \Phi^1_P$ (ML/s)	2.04	1.762	1.447	2.11	1.596
g_{As} (ML/s)	65	65	55	60	50
χ^1_{As}	0.0034	0.00662	0.0098	0.020	0.022
g_P (ML/s)	200	200	200	200	200
χ^1_P	0.0091	0.0068	0.0045	0.0045	0.0025
Reverse transition from $GaAs_xP_{1-x}$ to GaP					
Φ^0_P (ML/s)	1.817	1.362	0.907	0.91	0.496
Φ^1_P (ML/s)	1.362	1.362	1.362	1.362	1.362
Φ^0_{As} (ML/s)	0.224	0.336	0.448	1.12	1.224
Φ^1_{As} (ML/s)	0	0	0	0	0

Table 3. Fitting parameters for GaP/$GaAs_xP_{1-x}$/GaP NW HSs in Figure 6 with desorption.

Direct Transition from Pure GaP to $GaAs_xP_{1-x}$					
As/P flux ratio	0.5	1	2	5	10
v (ML/s)	2.5	2.5	2.5	5	5
x_0	0	0	0	0	0
x_1	0.0927	0.232	0.367	0.549	0.65
Reverse transition from $GaAs_xP_{1-x}$ to pure GaP					
v (ML/s)	1.25	1.25	1.25	1.25	1.25
$\Delta\xi_c = v/\gamma g_{As}$ (MLs)	40	40	35	45	45
ω	2	2	2	2	2

According to Figures 6 and 7, all models considered provided reasonable fits to the data. Figure 6 clearly demonstrates the narrowing effect in GaAsP NW HSs, which started from ternary $GaAs_{0.6}P_{0.4}$ stems, as discussed above (see Figure 2) and in Ref. [52]. The fits of the sharp NW HSs $GaAs_{0.6}P_{0.4}$/GaAs/$GaAs_{0.6}P_{0.4}$ of Ref. [36] in Figure 7 using the model of Ref. [52] and using the model of this work were almost indistinguishable. The reverse interface in the transition from pure GaAs to $GaAs_{0.6}P_{0.4}$ was broader than in the direct transition. This was explained by the higher stability of As atoms in liquid Ga relative to P atoms, which was why the removal of As atoms took more time [36,52]. Considering the fits to the compositional profiles of GaP/$GaAs_xP_{1-x}$/GaP NW HSs in Figure 6a, we believe that the curves with the desorption of both group V atoms at $c_g = 1$ were closer to reality and were obtained for the experimental axial growth rates at each

transition. The fits without desorption at $c_g = 0.247$ underestimated the axial growth rates for large As fractions in vapor, as discussed above. From Figure 7, the compositional profiles at the direct transition from GaP to $GaAs_xP_{1-x}$ were better fitted with the model of Ref. [52], while the reverse interfaces were better fitted with the model of this work. The model of Ref. [52] obviously overestimated the interfacial widths for all reverse transitions. In Ref. [52], we also used the Langmuir–McLean liquid–solid distribution, and obtained the fits shown in Figure 6 at $c_l = 0.1$. According to Table 2, the best fits to the same data using the model without desorption were obtained at $g_P = 200$ ML/s and $g_{As} = 50$–65 ML/s, yielding $c_l = g_{As}/g_P$ from 0.25 to 0.325. In the model with desorption, from $\Delta\xi_c = v/\gamma g_A \cong 40$ MLs and $\gamma = 0.000758$, we obtained $g_A \cong 41$ and, hence, $c_l \cong 0.2$. Therefore, all models predicted a faster transfer of P atoms from Ga liquid to solid relative to As atoms, with c_l ranging from 0.1 to ~0.3.

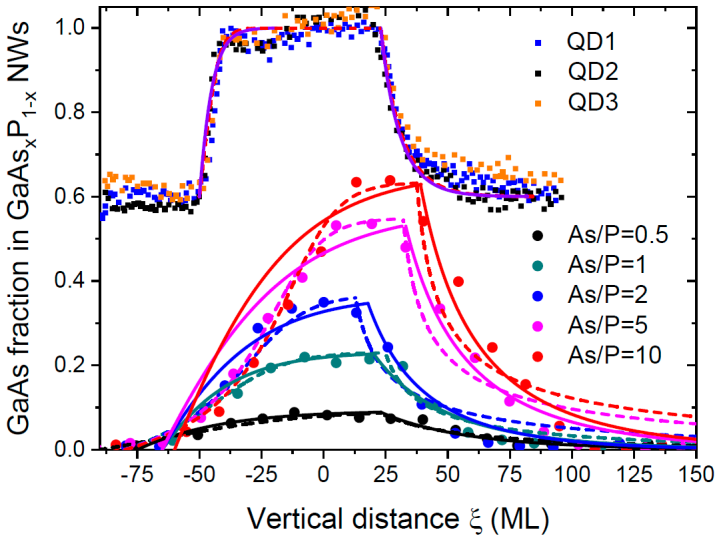

Figure 7. Same data as in Figure 6a for double NW HSs GaP/GaAsP/GaP with different compositions of GaAs obtained under different As/P ratios, as shown in the legend [35], along with much sharper NW HSs $GaAs_{0.6}P_{0.4}$/GaAs/$GaAs_{0.6}P_{0.4}$ for three GaAs quantum dots QD1, Q2 and QD3, obtained in Ref. [36] using very similar Ga-catalyzed MBE process (symbols). Dashed lines show the fits of Ref. [52]. Solid lines are the fits obtained within our model with desorption. The fits using the model of Ref. [52] and using the model of this work for the sharp NW HSs of Ref. [36] were almost indistinguishable.

6. Conclusions

In conclusion, a self-consistent model for compositional profiles across VLS III–V NW HSs based on the group V interchange was developed. The model essentially relied on only one assumption on the linear dependence of the crystallization rates of AC and BC pairs on the concentrations χ_A and χ_B, which automatically led to the Langmuir–McLean liquid–solid distribution. The quadratic dependence of the desorption rates of A and B atoms on their concentrations should have held regardless of the growth catalyst [13]. No further simplifications, such as $\chi_A + \chi_B = \text{const}$ in Ref. [52], were used in our treatment. The model allowed for the accumulation or depletion of group V atoms in liquid and the treatment of different non-stationary processes such as emptying the droplet upon the growth interruption. Simple analytical solutions obtained for the time-dependent concentrations of group V elements in the droplet, liquid and solid composition and the height of a HS provided the full description of the growth process. However, the coordinate-dependent compositional profile was obtained only implicitly. The model fit quite well the data on axial NW HSs in the GaAsP system and could be extended to other III–V ternary materials. The unknown crystallization rates of AC and BC pairs at the growth interface could be deduced from fitting the data on the interfacial profiles in III–V NW HSs.

We revealed some general properties of VLS NW HSs based on the group V interchange and their interfacial abruptness. In particular, the interfaces of VLS $A_xB_{1-x}C$ NW HSs with a more stable group V element A greatly improved if started from ternary $A_xB_{1-x}C$ and transitioned to pure AC rather than starting from pure BC and transitioning it to ternary $A_xB_{1-x}C$. Higher desorption rates of both group V elements suppressed the interfacial broadening due to the reservoir effect because the desorbed species did not contribute into crystallization at the growth interface. These factors should have been carefully considered in the growth experiments and could be used for obtaining a more abrupt interface in VLS NW HSs. The presented approach required refinements in several respects, such as including the rejected species and, hence, pseudo-binary interactions in solid and miscibility gaps [42,43,50], as well as treating the NW monolayer progression with the depletion of group V atoms and a possible "stopping size", where the supersaturation of liquid drops to zero [13,61]. This process was extremely complex even for binary VLS III–V NWs. We plan to consider these interesting effects and their impact on the compositional profiles in III–V NW HSs in forthcoming work.

Funding: The author acknowledges St. Petersburg State University for the research project no. 95440344.

Data Availability Statement: Data are contained within the article.

Conflicts of Interest: The author declares no conflict of interest.

References

1. Ning, C.-Z.; Dou, L.; Yang, P. Bandgap engineering in semiconductor alloy nanomaterials with widely tunable compositions. *Nat. Rev. Mater.* **2017**, *2*, 17070. [CrossRef]
2. McIntyre, P.C.; Fontcuberta i Morral, A. Semiconductor nanowires: To grow or not to grow? *Mater. Today Nano* **2020**, *9*, 100058. [CrossRef]
3. Boras, G.; Yu, X.; Liu, H. III–V ternary nanowires on Si substrates: Growth, characterization and device applications. *J. Semicond.* **2019**, *40*, 101301. [CrossRef]
4. Martelli, F. III-V ternary nanowires. In *Advances in III-V Semiconductor Nanowires and Nanodevices*; Li, J., Wang, D., LaPierre, R.R., Eds.; Bentham Science: Sharjah, United Arab Emirates, 2011; pp. 105–128.
5. Johansson, J.; Dick, K.A. Recent advances in semiconductor nanowire heterostructures. *CrystEngComm* **2011**, *13*, 7175. [CrossRef]
6. Hyun, J.K.; Zhang, S.; Lauhon, L.J. Nanowire heterostructures. *Ann. Rev. Mater. Res.* **2013**, *43*, 451. [CrossRef]
7. Glas, F. Critical dimensions for the plastic relaxation of strained axial heterostructures in free-standing nanowires. *Phys. Rev. B* **2006**, *74*, 121302. [CrossRef]
8. Singh, R.; Bester, G. Nanowire quantum dots as an ideal source of entangled photon pairs. *Phys. Rev. Lett.* **2009**, *103*, 063601. [CrossRef] [PubMed]
9. Leandro, L.; Gunnarsson, C.P.; Reznik, R.; Jöns, K.D.; Shtrom, I.; Khrebtov, A.; Kasama, T.; Zwiller, V.; Cirlin, G.; Akopian, N. Nanowire quantum dots tuned to atomic resonances. *Nano Lett.* **2018**, *18*, 7217. [CrossRef] [PubMed]
10. Dalacu, D.; Poole, P.J.; Williams, R.L. Nanowire-based sources of non-classical light. *Nanotechnology* **2019**, *30*, 232001. [CrossRef]
11. Wagner, R.S.; Ellis, W.C. Vapor-liquid-solid mechanism of single crystal growth. *Appl. Phys. Lett.* **1964**, *4*, 89. [CrossRef]
12. Colombo, C.; Spirkoska, D.; Frimmer, M.; Abstreiter, G.; Fontcuberta i Morral, A. Ga-assisted catalyst-free growth mechanism of GaAs nanowires by molecular beam epitaxy. *Phys. Rev. B* **2008**, *77*, 155326. [CrossRef]
13. Dubrovskii, V.G.; Glas, F. Vapor–liquid–solid growth of semiconductor nanowires. In *Fundamental Properties of Semiconductor Nanowires*; Fukata, N., Rurali, R., Eds.; Springer: Singapore, 2020. [CrossRef]
14. Borg, B.M.; Dick, K.A.; Eymery, J.; Wernersson, L.-E. Enhanced Sb incorporation in InAsSb nanowires grown by metalorganic vapor phase epitaxy. *Appl. Phys. Lett.* **2011**, *98*, 113104. [CrossRef]
15. Namazi, L.; Ghalamestani, S.G.; Lehmann, S.; Zamani, R.R.; Dick, K.A. Direct nucleation, morphology and compositional tuning of $InAs_{1-x}Sb_x$ nanowires on InAs (111)B substrates. *Nanotechnology* **2017**, *28*, 165601. [CrossRef] [PubMed]
16. Zhuang, Q.D.; Alradhi, H.; Jin, Z.M.; Chen, X.R.; Shao, J.; Chen, X.; Sanchez, A.M.; Cao, Y.C.; Liu, J.Y.; Yates, P.; et al. Optically-efficient InAsSb nanowires for silicon-based mid-wavelength infrared optoelectronics. *Nanotechnology* **2017**, *28*, 105710. [CrossRef] [PubMed]
17. Wen, L.; Pan, D.; Liu, L.; Tong, S.; Zhuo, R.; Zhao, J. Large-composition-range pure-phase homogeneous $InAs_{1-x}Sb_x$ nanowires. *J. Phys. Chem. Lett.* **2022**, *13*, 598. [CrossRef] [PubMed]
18. Ek, M.; Borg, B.M.; Johansson, J.; Dick, K.A. Diameter limitation in growth of III-Sb-containing nanowire heterostructures. *ACS Nano* **2013**, *7*, 3668. [CrossRef] [PubMed]
19. Yuan, X.; Caroff, P.; Wong-Leung, J.; Tan, H.H.; Jagadish, C. Controlling the morphology, composition and crystal structure in gold-seeded $GaAs_{1-x}Sb_x$ nanowires. *Nanoscale* **2015**, *7*, 4995. [CrossRef] [PubMed]

20. Dheeraj, D.L.; Patriarche, G.; Zhou, H.; Harmand, J.C.; Weman, H.; Fimland, B.O. Growth and structural characterization of GaAs/GaAsSb axial heterostructured nanowires. *J. Cryst. Growth* **2009**, *311*, 1847. [CrossRef]
21. Ren, D.; Ahtapodov, L.; Nilsen, J.S.; Yang, J.; Gustafsson, A.; Huh, J.; Conibeer, G.J.; Van Helvoort, A.T.; Fimland, B.O.; Weman, H. Single-mode near-infrared lasing in a GaAsSb-based nanowire superlattice at room temperature. *Nano Lett.* **2018**, *18*, 2304. [CrossRef]
22. Plissard, S.; Dick, K.A.; Wallart, X.; Caroff, P. Gold-free GaAs/GaAsSb heterostructure nanowires grown on silicon. *Appl. Phys. Lett.* **2010**, *96*, 121901. [CrossRef]
23. Tchernycheva, M.; Cirlin, G.E.; Patriarche, G.; Travers, L.; Zwiller, V.; Perinetti, U.; Harmand, J.C. Growth and characterization of InP nanowires with InAsP insertions. *Nano Lett.* **2007**, *7*, 1500. [CrossRef] [PubMed]
24. Persson, A.I.; Bjork, M.T.; Jeppesen, S.; Wagner, J.B.; Wallenberg, L.R.; Samuelson, L. $InAs_{1-x}P_x$ nanowires for device engineering. *Nano Lett.* **2006**, *6*, 403. [CrossRef] [PubMed]
25. Tateno, K.; Zhang, G.; Takiguchi, M.; Gotoh, H.; Sogawa, T. VLS growth of alternating InAsP/InP heterostructure nanowires for multiple-quantum-dot structures. *Nano Lett.* **2012**, *12*, 2888. [CrossRef] [PubMed]
26. Mandl, B.; Keplinger, M.; Messing, M.E.; Kriegner, D.; Wallenberg, R.; Samuelson, L.; Bauer, G.; Stangl, J.; Holy, V.; Deppert, K. Self-seeded axio-radial InAs-$InAs_{1-x}P_x$ nanowire heterostructures beyond "common" VLS growth. *Nano Lett.* **2018**, *18*, 144. [CrossRef] [PubMed]
27. Zannier, V.; Rossi, F.; Dubrovskii, V.G.; Ercolani, D.; Battiato, S.; Sorba, L. Nanoparticle stability in axial InAs−InP nanowire heterostructures with atomically sharp interfaces. *Nano Lett.* **2018**, *18*, 167. [CrossRef] [PubMed]
28. Haffouz, S.; Zeuner, K.D.; Dalacu, D.; Poole, P.J.; Lapointe, J.; Poitras, D.; Mnaymneh, K.; Wu, X.; Couillard, M.; Korkusinski, M.; et al. Bright single InAsP quantum dots at telecom wavelengths in position-controlled InP nanowires: The role of the photonic waveguide. *Nano Lett.* **2018**, *18*, 3047. [CrossRef] [PubMed]
29. Zannier, V.; Rossi, F.; Ercolani, D.; Sorba, L. Growth dynamics of InAs/InP nanowire heterostructures by Au-assisted chemical beam epitaxy. *Nanotechnology* **2019**, *30*, 094003. [CrossRef] [PubMed]
30. Zhang, Y.; Aagesen, M.; Holm, J.V.; Jørgensen, H.I.; Wu, J.; Liu, H. Self-catalyzed GaAsP nanowires grown on silicon substrates by solid-source molecular beam epitaxy. *Nano Lett.* **2013**, *13*, 3897. [CrossRef] [PubMed]
31. Zhang, Y.; Sanchez, A.M.; Sun, Y.; Wu, J.; Aagesen, M.; Huo, S.; Kim, D.; Jurczak, P.; Xu, X.; Liu, H. Influence of droplet size on the growth of self-catalyzed ternary GaAsP nanowires. *Nano Lett.* **2016**, *16*, 1237. [CrossRef]
32. Himwas, C.; Collin, S.; Rale, P.; Chauvin, N.; Patriarche, G.; Oehler, F.; Julien, F.H.; Travers, L.; Harmand, J.C.; Tchernycheva, M. In situ passivation of GaAsP nanowires. *Nanotechnology* **2017**, *28*, 495707. [CrossRef]
33. Priante, G.; Patriarche, G.; Oehler, F.; Glas, F.; Harmand, J.C. Abrupt GaP/GaAs interfaces in self-catalyzed nanowires. *Nano Lett.* **2015**, *15*, 6036. [CrossRef] [PubMed]
34. Boulanger, J.P.; LaPierre, R.R. Unveiling transient GaAs/GaP nanowire growth behavior using group V oscillations. *Cryst. Growth* **2014**, *388*, 116–123. [CrossRef]
35. Bolshakov, A.D.; Fedorov, V.V.; Sibirev, N.V.; Fetisova, M.V.; Moiseev, E.I.; Kryzhanovskaya, N.V.; Koval, O.Y.; Ubyivovk, E.V.; Mozharov, A.M.; Cirlin, G.E.; et al. Growth and characterization of GaP/GaPAs nanowire heterostructures with controllable composition. *Phys. Stat. Sol. RRL* **2019**, *13*, 1900350. [CrossRef]
36. Zhang, Y.; Velichko, A.V.; Fonseka, H.A.; Parkinson, P.; Gott, J.A.; Davis, G.; Aagesen, M.; Sanchez, A.M.; Mowbray, D.; Liu, H. Defect-free axially-stacked GaAs/GaAsP nanowire quantum dots with strong carrier confinement. *Nano Lett.* **2021**, *21*, 5722. [CrossRef] [PubMed]
37. Paladugu, M.; Zou, J.; Guo, Y.-N.; Zhang, X.; Kim, Y.; Joyce, H.J.; Gao, Q.; Tan, H.H.; Jagadish, C. Nature of heterointerfaces in GaAs/InAs and InAs/GaAs axial nanowire heterostructures. *Appl. Phys. Lett.* **2008**, *93*, 101911. [CrossRef]
38. Heiß, M.; Gustafsson, A.; Conesa-Boj, S.; Peiró, F.; Morante, J.R.; Abstreiter, G.; Arbiol, J.G.; Samuelson, L.; Fontcuberta i Morral, A. Catalyst-free nanowires with axial $In_xGa_{1-x}As$/GaAs heterostructures. *Nanotechnology* **2009**, *20*, 075603. [CrossRef]
39. Priante, G.; Glas, F.; Patriarche, G.; Pantzas, K.; Oehler, F.; Harmand, J.C. Sharpening the interfaces of axial heterostructures in self-catalyzed AlGaAs nanowires: Experiment and theory. *Nano Lett.* **2016**, *16*, 1917. [CrossRef]
40. Sjokvist, R.; Jacobsson, D.; Tornberg, M.; Wallenberg, R.; Leshchenko, E.D.; Johansson, J.; Dick, K.A. Compositional correlation between the nanoparticle and the growing Au-assisted $I_xGa_{1-x}As$ nanowire. *J. Phys. Chem. Lett.* **2021**, *12*, 7590. [CrossRef]
41. Dick, K.A.; Bolinsson, J.; Borg, B.M.; Johansson, J. Controlling the abruptness of axial heterojunctions in III–V nanowires: Beyond the reservoir effect. *Nano Lett.* **2012**, *12*, 3200. [CrossRef]
42. Ghasemi, M.; Leshchenko, E.D.; Johansson, J. Assembling your nanowire: An overview of composition tuning in ternary III–V nanowires. *Nanotechnology* **2021**, *32*, 072001. [CrossRef]
43. Leshchenko, E.D.; Dubrovskii, V.G. An overview of modeling approaches for compositional control in III–V ternary nan-owires. *Nanomaterials* **2023**, *13*, 1659. [CrossRef] [PubMed]
44. Dubrovskii, V.G.; Sibirev, N.V. Factors influencing the interfacial abruptness in axial III-V nanowire heterostructures. *Cryst. Growth Des.* **2016**, *16*, 2019. [CrossRef]
45. Glas, F. Comparison of modeling strategies for the growth of heterostructures in III–V nanowires. *Cryst. Growth Des.* **2017**, *17*, 4785. [CrossRef]
46. Dubrovskii, V.G.; Koryakin, A.A.; Sibirev, N.V. Understanding the composition of ternary III-V nanowires and axial nanowire heterostructures in nucleation-limited regime. *Mater. Design* **2017**, *132*, 400. [CrossRef]

47. Johansson, J.; Ghasemi, M. Kinetically limited composition of ternary III-V nanowires. *Phys. Rev. Mater.* **2017**, *1*, 040401.
48. Leshchenko, E.D.; Johansson, J. Role of thermodynamics and kinetics in the composition of ternary III-V nanowires. *Nanomaterials* **2020**, *10*, 2553. [CrossRef] [PubMed]
49. Dubrovskii, V.G. Liquid-solid and vapor-solid distributions of vapor-liquid-solid III-V ternary nanowires. *Phys. Rev. Mater.* **2023**, *7*, 096001. [CrossRef]
50. Dubrovskii, V.G. Circumventing the uncertainties of the liquid phase in the compositional control of VLS III–V ternary nanowires based on group V intermix. *Nanomaterials* **2024**, *14*, 207. [CrossRef]
51. McLean, D. *Grain Boundaries in Metals*; Oxford University Press: New York, NY, USA, 1957.
52. Dubrovskii, V.G. Interfacial profiles in VLS III-V axial nanowire heterostructures based on group V interchange. *Phys. Rev. Mater.* **2024**. *submitted*.
53. Glas, F.; Ramdani, M.R.; Patriarche, G.; Harmand, J.C. Predictive modeling of self-catalyzed III-V nanowire growth. *Phys. Rev. B* **2013**, *88*, 195304. [CrossRef]
54. Cirlin, G.E.; Dubrovskii, V.G.; Sibirev, N.V.; Soshnikov, I.P.; Samsonenko, Y.B.; Tonkikh, A.A.; Ustinov, V.M. The diffusion mechanism in the formation of GaAs and AlGaAs nanowhiskers during the process of molecular-beam epitaxy. *Semiconductors* **2005**, *39*, 557. [CrossRef]
55. Plante, M.C.; LaPierre, R.R. Analytical description of the metal-assisted growth of III–V nanowires: Axial and radial growths. *J. Appl. Phys.* **2009**, *105*, 114304. [CrossRef]
56. Harmand, J.C.; Glas, F.; Patriarche, G. Growth kinetics of a single $InP_{1-x}As_x$ nanowire. *Phys. Rev. B* **2010**, *81*, 235436. [CrossRef]
57. Borg, M.; Johansson, J.; Storm, K.; Deppert, K. Geometric model for metalorganic vapour phase epitaxy of dense nanowire arrays. *J. Cryst. Growth* **2013**, *366*, 15. [CrossRef]
58. Metaferia, W.; Persson, A.R.; Mergenthaler, K.; Yang, F.; Zhang, W.; Yartsev, A.; Wallenberg, R.; Pistol, M.E.; Deppert, K.; Samuelson, L.; et al. GaAsP nanowires grown by aerotaxy. *Nano Lett.* **2016**, *16*, 5701. [CrossRef]
59. Samuelson, L.; Omling, P.; Grimmeiss, H.G. Alloying mechanisms in MOVPE $GaAs_{1-x}P_x$. *J. Cryst. Growth* **1983**, *61*, 425. [CrossRef]
60. Ansara, I.; Chatillon, C.; Lukas, H.L.; Nishizawa, T.; Ohtani, H.; Ishida, K.; Hillert, M.; Sundman, B.; Argent, B.B.; Watson, A.; et al. A binary database for III–V compound semiconductor systems. *Calphad* **1994**, *18*, 177. [CrossRef]
61. Glas, F.; Panciera, F.; Harmand, J.C. Statistics of nucleation and growth of single monolayers in nanowires: Towards a deterministic regime. *Phys. Status Solidi RRL* **2022**, *16*, 2100647. [CrossRef]